ACS APPLIED NANO MATERIALS
Cite This: ACS Appl. Nano Mater. 2019, 2, 3262−3270
Article
www.acsanm.org

Electron-Beam-Driven Structure Evolution of Single-Layer $MoTe_2$ for Quantum Devices

Tibor Lehnert,*[,†] Mahdi Ghorbani-Asl,[‡] Janis Köster,[†] Zhongbo Lee,[†] Arkady V. Krasheninnikov,[‡,§] and Ute Kaiser*[,†]

[†]Electron Microscopy Group of Materials Science, Ulm University, Albert-Einstein-Allee 11, 89081 Ulm, Germany
[‡]Institute of Ion Beam Physics and Materials Research, Helmholtz-Zentrum Dresden-Rossendorf, 01328 Dresden, Germany
[§]Department of Applied Physics, Aalto University, 00076 Aalto, Finland

Supporting Information

ABSTRACT: The 40 kV high-resolution transmission electron microscopy (TEM) experiments are performed to understand defect formation and evolution of their atomic structure in single-layer 2H $MoTe_2$ under electron beam irradiation. We show that Te vacancies can agglomerate either in single Te vacancy lines or in extended defects composed of column Te vacancies, including rotational trefoil-like defects, with some of them being never reported before. The formation of inversion domains with mirror twin boundaries of different types, along with the islands of the metallic T′ phase was also observed. Our first-principles calculations provide insights into the energetics of the transformations as well as the electronic structure of the system with defects and point out that some of the observed defects have localized magnetic moments. Our results indicate that various nanoscale structures, including metallic quantum dots consisting of T′ phase islands and one-dimensional metallic quantum systems such as vacancy lines and mirror twin boundaries embedded into a semiconducting host material can be realized in single-layer 2H $MoTe_2$, and defect-associated magnetism can also be added, which may allow prospective control of optical and electronic properties of two-dimensional materials.

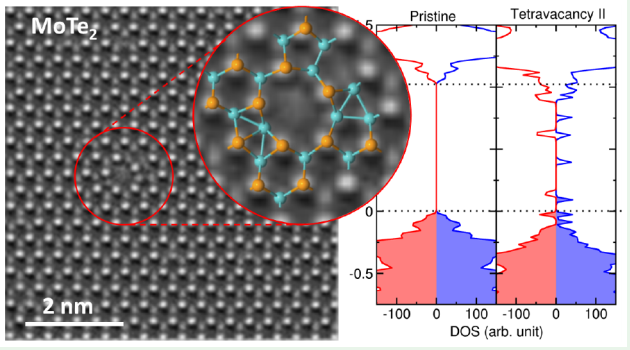

KEYWORDS: *defects, 2D $MoTe_2$, transmission electron microscopy, transition metal dichalcogenide, DFT, quantum devices*

INTRODUCTION

Transition metal dichalcogenides (TMDs) with a general structural formula MX_2, where M stands for a transition metal (e.g., Mo. W, Re) and X for chalcogen atoms (S, Se, Te) are layered materials, which can, depending on the constituent chemical elements, be insulators, semiconductors, metals, superconductors, or charge density waves.[1−4] Single structural units (sheets) of TMDs can be produced by exfoliation[1] or grown by chemical vapor deposition,[5] and these two-dimensional (2D) systems have been shown[5−8] to possess many interesting properties with numerous implications for potential applications such as atomic defect based quantum emitters or spin qubit based quantum wires.[9−11] Moreover, even for the same chemical composition, these compounds exist in several crystalline phases with drastically different properties.[3,6−8] For example, the hexagonal 2H phase in Mo-containing TMDs is normally semiconducting, while the metastable monoclinic (1T′) phase is metallic.

Among TMDs, $MoTe_2$ is one of the most interesting materials, as the energy difference between its 2H and 1T′ phases is very small (∼31 meV per formula unit),[12] and the transformation from the 2H to 1T phase can be rather easily induced by electrostatic doping[13] or laser processing.[14] The precise control of the atomic structure offers opportunities for engineering the electronic properties,[15] device fabrication,[14] and catalysis.[16] Moreover, the properties of $MoTe_2$ can further be tuned by a controllable introduction of defects. Vacancies were shown[14] to facilitate a transition from the H to T phase and be efficient catalytic centers.[16,17] Metal vacancies and chalcogen-metal antisites were demonstrated to promote magnetism, thus adding functionalities to this system.[18]

Agglomeration of defects, either vacancies or Mo interstitials, can give rise to the formation of inversion domains and associated mirror twin boundaries (MTBs),[15,19,20] which can exhibit very peculiar behavior,[21] as one-dimensional metallic quantum objects confined into a semiconducting matrix. Inversion domains with MTBs can be formed in 2D TMDs under electron irradiation in a transmission electron microscope (TEM) utilizing the electron beam both as an imaging tool and a means to functionalize the material[20,22,23] or by

Received: April 3, 2019
Accepted: April 26, 2019
Published: April 26, 2019

DOI: 10.1021/acsanm.9b00616
ACS Appl. Nano Mater. 2019, 2, 3262−3270

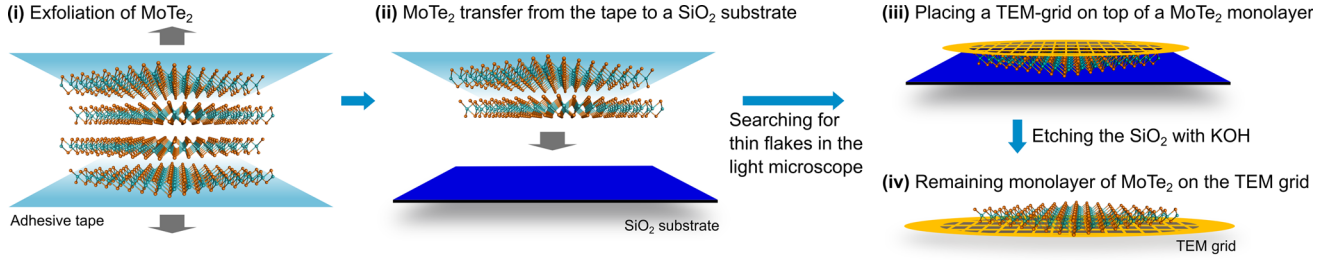

Figure 1. Fabrication process of a freestanding $MoTe_2$ monolayer via exfoliation for TEM investigations.

depositing extra Mo atoms at elevated temperatures.[24] As compared to other TMDs, the formation of a dense network of inversion domains is particularly easy in $MoTe_2$ due to its larger unit cell size as compared to other Mo based TMDs, which makes the interstitial site more accessible for extra atoms.[24]

However, in spite of a few theoretical and experimental works on $MoTe_2$[25−27] and other TMDs,[23,27−34] neither the mechanism of the formation of these defects nor their evolution under the electron beam is fully understood. The atomic structure[15] of the emerging MTBs appear to depend on the material and experimental conditions, and electron irradiation sometimes gives rise to the development of vacancy lines but not MTBs.[23,25,32,33] It is not clear what role point defects play in MTB formation or how mechanical strain affects this process. The exact structure and directions (armchair, zigzag) of the line defects can be quite different,[29,32] and the reason for this observation remains elusive, partly because contrast and resolution are limited in conventional spherical aberration-corrected TEMs.

Here, we use not only spherical (Cs), but also chromatic (Cc) aberration-corrected high-resolution (HR) TEM at an electron acceleration voltage of 40 kV, resulting in increased resolution and contrast,[35−37] to get microscopic insights into defect appearance and evolution under electron beam in 2D $MoTe_2$. We combine our Cc/Cs-corrected HRTEM experiments with first-principles calculations carried out within the framework of the density functional theory (DFT) to systematically study defect formation, migration, and coalescence. We follow the transformations atom-by-atom and show that single tellurium vacancies agglomerate either in short vacancy lines, extended trefoil-like defects, and ultimately form inversion domains. Our theoretical data on magnetic and electronic properties of electron-beam modified $MoTe_2$ show that certain functionalities can be added to the system, such as quantum dots and quantum wires, through a controllable introduction of particular defects, which lead to application-related control of optical, electronic, and magnetic properties of 2D TMDs.

EXPERIMENTAL SECTION

Sample Preparation. Molybdenum ditelluride monolayers were exfoliated via an adhesive tape on silicon dioxide substrates with thickness of 90 nm as it is shown in Figure 1, (i) and (ii). With an optical microscope, monolayers were identified due to contrast measurements and compared to calculations with the Fresnel formula,[38,39] which yields to a contrast of ∼46% for a monolayer of $MoTe_2$ on 90 nm SiO_2 illuminated with green light. After a monolayer is located, a Quantifoil TEM grid R 1.2/1.3 is placed with a drop of isopropyl alcohol on top. Because of the evaporation of the isopropyl alcohol, the grid comes into contact with the flake (iii). With a drop of potassium hydroxide (KOH), the SiO_2 is etched away and therefore releases the grid with the $MoTe_2$ flake (iv). Afterward, the residues of the preparation are removed with double distilled water. Although some regions in the single-layer $MoTe_2$ are contaminated, there are still sufficient clean areas for the TEM investigations.

TEM Conditions. The high-resolution TEM images were acquired at the Cc/Cs-corrected Sub-Angström Low-Voltage Electron microscope (SALVE) at a voltage of 40 kV. Measured values for Cc and Cs were in the range of −10 μm to −20 μm. The vacuum in the column of the TEM was in the range of 10^{-5} Pa. Dose rates in the range of 10^6 e^-/nm^2 s were used, and the images were recorded on a 4k × 4k camera with exposure times of 1 s.

Image Simulations. The image calculation has employed the following experimental parameters: A focal spread of 0.5 nm, an image spread of 30 pm, a convergence angle of 0.1 mrad, and a sampling of 0.16 Å/pixel to account for the influence of the CCD camera. Furthermore, the fifth-order spherical aberration C5 was set to 1.8 mm and the following aberration coefficients were optimized and used for the image calculation: a defocus of 7.5 nm and third-order spherical aberration coefficient Cs of −8.2 μm.

Computational Methods. The density functional theory calculations have been performed based on the generalized gradient approximation (GGA) with Perdew−Burke−Ernzerhof (PBE)[40] for exchange-correlation function as implemented in VASP code.[41] The atomic structures of $MoTe_2$ monolayers with various defects have been fully optimized using 10 × 10 supercells. The maximum force during the optimization was set to be less than 0.01 eV/Å. A plane-wave basis set with an energy cutoff of 400 eV is used. The Brillouin zone of the supercells was sampled using 4 × 4 × 1 k-points for optimization according to the scheme proposed by Monkhorst and Pack.[42] Formation energies of defects have been calculated as $E_f = E_{def} - (E_{pristine} - \mu_x)$, where E_{def} is the energy of the system containing defect and $E_{pristine}$ is the energies of the pristine system. μ_x stands for the chemical potential of the X species, which is taken as the spin-polarized energy of the isolated atom.

RESULTS AND DISCUSSIONS

Figure 2 shows a 40 kV Cc/Cs-corrected high-resolution (HR)TEM image in bright atom contrast where differences between the contrast of a single missing Te atom (Te vacancy) and two missing Te atoms (Te divacancy-column) can be clearly seen as marked in (a) by the green and blue arrows, respectively. It should be noted that sub-Ångström resolution (0.9 Å) is achievable at 40 kV electron accelerating voltage, and our technique allows a fully atomic position-corrected image acquisition within a short time scale (∼1 s) over a large field of view.[36] Any ballistic damage should be excluded at 40 kV due to high mass of Te and Mo atoms,[43] the maximum transferrable kinetic energy is 0.72 and 0.95 eV for the Te and Mo atoms, respectively. This is far below the formation energy for a Te vacancy (4.87 eV) and Mo vacancy (10.45 eV). We stress that the displacement thresholds are generally higher than the formation energies because a part of the deposited energy can be transferred to the atoms neighboring the recoil atom, which in addition to that may also need to overcome a

DOI: 10.1021/acsanm.9b00616
ACS Appl. Nano Mater. 2019, 2, 3262−3270

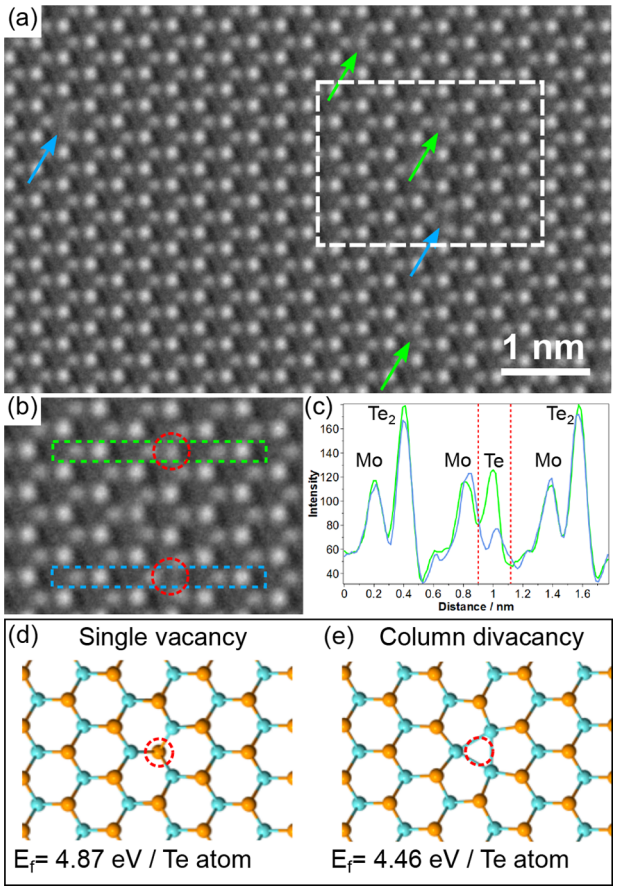

Figure 2. The 40 kV raw data of Cc/Cs-corrected high-resolution TEM images of $MoTe_2$ is shown in (a) with different defects in bright atom contrast. A column of two Te atoms is brighter than one Mo atom. Single Te vacancies are marked with green arrows and column Te divacancies with blue ones. In the case of one missing Te atom, the contrast between the remaining Te is comparable to the contrast of the neighboring Mo atoms, which can be seen in the green line scan in (b). For column Te divacancies, the contrast vanishes as seen from the blue line-scan (c). (d) DFT-optimized structure of a single Te vacancy with the corresponding formation energy. The red dashed circles mark the position of missing Te atoms. Image (e) is the structure simulation of a column Te divacancy. Turquoise balls stand for Mo and orange ones for Te atoms.

potential barrier.[43] However, the electron beam is responsible for vacancy production. Figure S1 in the Supporting Information (SI) shows the increasing vacancy concentration from ~0.17 vacancies/nm^2 to ~0.27 vacancies/nm^2 after a total accumulated dose of ~1.2 × 10^9 e^-/nm^2. The exact mechanism of defect formation is not known, but it is likely beam-induced chemical etching[44] resulting from the reactive species, e.g., fragments of water and other molecules present in the TEM column and thus on the sample surface, is responsible for the appearance of defects. Further damage accumulation likely proceeds through the localization of beam-induced electronic excitations on the existing defects resulting in the promotion of electrons into antibonding orbitals and bond-breaking.

As can be seen in Figure 2 a, single Te vacancies and column Te divacancies occur frequently in the lattice due to the interaction with the electron beam as shown previously for other TMDs such as MoS_2, $MoSe_2$, and $NbSe_2$.[29−31] The line scan region in Figure 2c, obtained from the dashed area in (b), indicates that one missing Te atom produces still a slightly higher signal than a neighboring Mo atom (the mass is 127.60 u for Te and 95.94 u for Mo), the green diagram in Figure 2c, and two missing Te atoms on top of each other (column divacancy) can be identified by the strongly reduced signal in the corresponding blue line-scan (see the framed area). The faint signal might result from neighboring Mo atoms, which slightly fall into with the line scan region. In addition, small contrast contribution is also a consequence of multiple scattering of the electron wave within the atomic layers of single-layer $MoTe_2$. This effect can introduce weak contrast within the fully stoichiometric rings.[45]

The appearance of point defects and the migration of Te atoms in $MoTe_2$ was observed earlier with STEM.[26] The authors reported also rotationally symmetric defects, as well as line defects such as mirror twin grain boundaries.[26] As we show below, the morphology of defects produced in TEM is somewhat different from those obtained in the STEM mode. However, the TEM mode allows fast image acquisition with a large field of view, thus the dynamics and transformations of point defects into rotational and extended defects can be studied in detail. Furthermore, bigger surrounding areas of the defects can be taken into account for understanding the electron-beam-induced evolution due to the large field of view, shown in Figure S1 in the SI.

In Figure 2d,e, structural models determined by DFT calculations are shown for a single vacancy (d) and a column divacancy, where two Te atoms on top of each other are missing (e). The calculated formation energies for a single Te vacancy and column divacancy are 4.87 and 4.46 eV per Te atom (in total E_f (Te_2) = 8.92 eV). These values are slightly lower than previously reported as different chemical potentials (with an account for spin polarization) of isolated atoms were used in the calculations.[43] Although it is energetically more favorable to have a column divacancy than two single vacancies, the system is not under equilibrium conditions, and besides, the defects may be preferentially produced on one side of the sheet only, which may explain why we see more single vacancies in our experiments. The formation energy of Mo vacancies was found to be E_f = 10.45 eV per Mo atom, which is much higher than for Te. This is in line with the observations that only Te vacancies and related defects were present in our samples.

As evident from Figure 3a−c, the formation of more complicated defects where several atoms are missing, was also observed. Within the red frames in the lower images, the atoms are marked with different colors (turquoise for Mo and orange for Te_2), which allows an easier comparison to the schematics of the transformation process presented in Figure 3d. In Figure S2 in the SI, image simulations of the of the more complicated defects are given. We call these structures "extended point defects", as they are between truly point defects, like single vacancies, and extended structures, like linear agglomerations of vacancies, which can be of infinite length. The formation of such defects starts with two column Te divacancies. Because of the migration of two Te atoms, which move into the center of the structure, a symmetric defect is formed, which we name tetravacancy I. As a guide for the eye, black dashed lines and arrows in Figure 3d indicate the distortion and migration of the atoms, respectively. The faint and slightly blurred contrast of the Mo atoms surrounding the Te_2 atom column in the center which appears in Figure 3a but not in Figure S2(a) in the SI, might be caused by vibrating Mo atoms, indicates that the

DOI: 10.1021/acsanm.9b00616
ACS Appl. Nano Mater. 2019, 2, 3262−3270

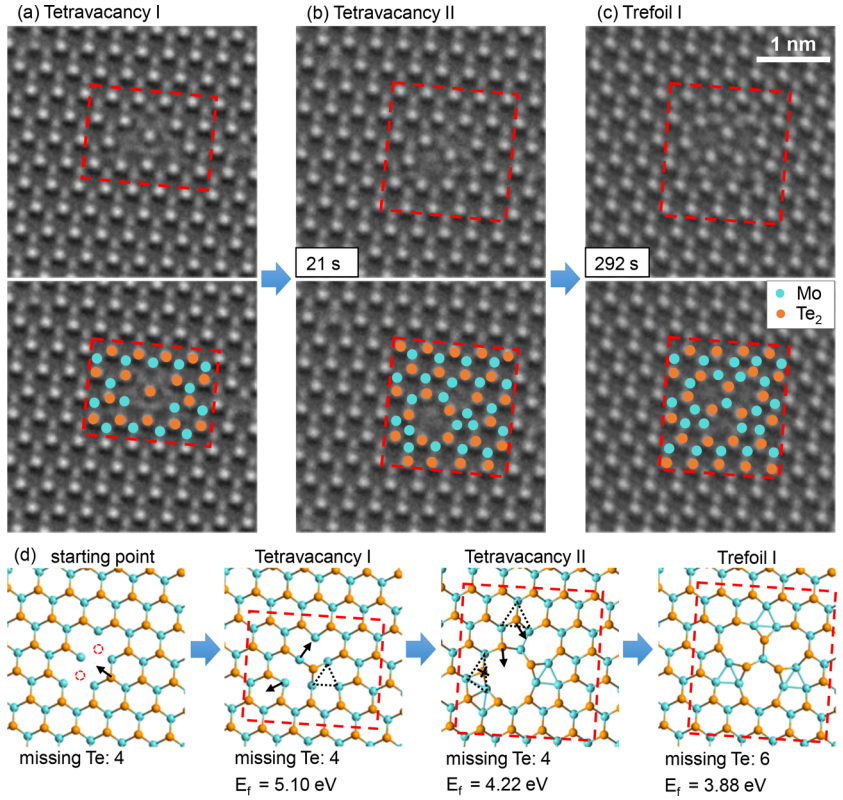

Figure 3. The 40 kV Cc/Cs-corrected HRTEM images of two-dimensional extended defects in $MoTe_2$ imaged in bright atom contrast. (a) Symmetrical tetravacancy I structure, (b) a distorted tetravacancy II structure which is formed after 21 s, and (c) the trefoil-like structure (trefoil I) after an additional 271 s. The dose rate was about 1.75×10^6 e^-/nm^2 s. Images below are identical, however, in the red-framed area atoms are marked: Mo atoms are turquoise and two Te atoms above each other are marked orange. The schematic representations in (d) show the corresponding structure simulations. Furthermore, the process of the experimental clustering of column divacancy is presented. Because of tellurium migration, the intermediate tetravacancy I forms from two column divacancies. Afterward, the tetravacancy I transforms into the stable tetravacancy II structure, and by forming further column Te divacancy, trefoil-like defect structures evolve (the given formation energies E_f are per Te atom).

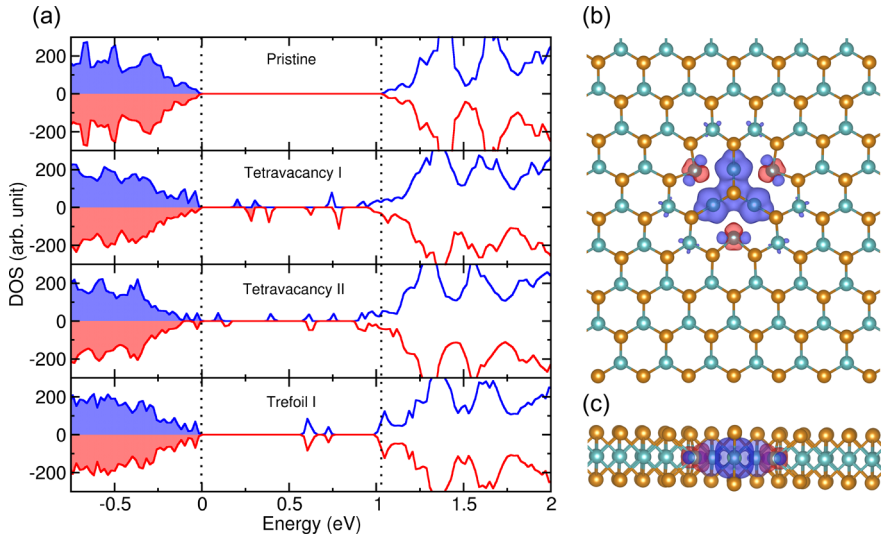

Figure 4. (a) Spin-polarized total density of states for various point extended defects in $MoTe_2$. The dotted lines show the band edges of the pristine system. (b,c) Majority/minority spin density of tetravacancy I, defined as $\rho_{up} - \rho_{down}$, where ρ_{up} and ρ_{down} are spin-resolved charge densities for spin-up and down components, top (b) and side (c) views. Blue and red colors correspond to majority/minority spin densities, respectively. The isosurface was set to 0.002 e $Å^{-3}$. The magnetic character of the tetravacancies I and II defects are clearly observable due to the asymmetric spin polarization effect in the band gap region.

tetravacancy I may be a metastable configuration. Indeed, a distortion takes place, and tetravacancy I turns into the distorted and more stable tetravacancy II configuration, Figure 3b. After further electron irradiation and additional Te_2

DOI: 10.1021/acsanm.9b00616
ACS Appl. Nano Mater. 2019, 2, 3262−3270

vacancy formation, the distorted tetravacancy II transforms into a symmetric trefoil-like defect structure (trefoil I), Figure 3c. Because of a bond rotation, other types of tetravacancy and trefoil defects can be formed such as tetravacancies III and IV and trefoil II. However, these structures are less favored due to the higher formation energy (see Figures S3 and S4 in the SI), which is in line with the experimental HRTEM observations.

To study the electronic and magnetic properties of various extended defects, the spin-polarized total density of states (DOS) was calculated and shown in Figure 4. The presence of defects significantly changes the electronic structure and introduces a large number of midgap states. The defect-associated midgap states are mostly localized around the defects, and thus the defects act as scattering centers affecting the electronic transport properties.[46] Moreover, due to the shift between the spin-up and spin−down states in the tetravacancy I and II configurations, these localized states have a magnetic character (cf Figure 4). While pristine $MoTe_2$ with the $4d^2$ configuration of Mo atoms is a nonmagnetic material,[47] our calculations showed a total magnetic moment of 4 μ_B and 2 μ_B for tetravacancy I and II configurations, respectively. Because of the locally changed electronic properties of the defect structures, embedded into a semiconducting matrix, they can be regarded as quantum dots. Similar behavior was also found for the less stable tetravacancy IV (Figure S5 in SI). It should be mentioned that a single Te vacancy exhibits negligible spin polarization. The spin density plot of tetravacancy I shows that the magnetism is mainly localized on the three Mo atoms surrounding the central Te atom, with some smaller contribution from the next adjacent Mo atoms. In the case of trefoil defects, the number of midgap states reduces when bonds are rotated and the system is nonmagnetic.

During subsequent TEM imaging, the interaction of the electron beam with the $MoTe_2$ specimen resulted also in line defect formation. Figure 5 shows an experimental 40 kV Cc/Cs-corrected HRTEM image of a single vacancy line, composed of four missing Te atoms (a) together with the calculated HRTEM image (b) based on relaxed atomic coordinates determined by DFT calculations. The best fit with the experiment was found when assuming a slight sample tilt of 4°, which could be caused by a nonperfect sample alignment. The lower panels of (a) and (b) are identical images, but for better defect visualization, the atoms within the red dashed area of the upper image are again marked with different colors: solid, orange dots mark two stacked-up Te (Te_2) atoms, orange rings mark one Te atom, and the blue solid dots mark Mo atoms, the single vacancy line is framed. The comparison of the atom positions between experimental and simulated images show qualitatively good agreement, with minor differences possibly originating from the mechanical strain present in the system and associated with the loss of atoms.

To understand line defect formations, DFT calculations were performed for different Te vacancy line structures and the atomic configurations are displayed together with their formation energies in Figure 6. Te vacancy lines are either oriented in the zigzag direction (cf Figure 6a−c) or along armchair direction (cf Figure 6e−g). In either of the directions, the Te vacancy line can have four possible structures: a single vacancy line, a column divacancy line, a staggered divacancy line, and finally there are three missing Te atoms perpendicular to the vacancy line direction (shown in Figure S6 in SI). The

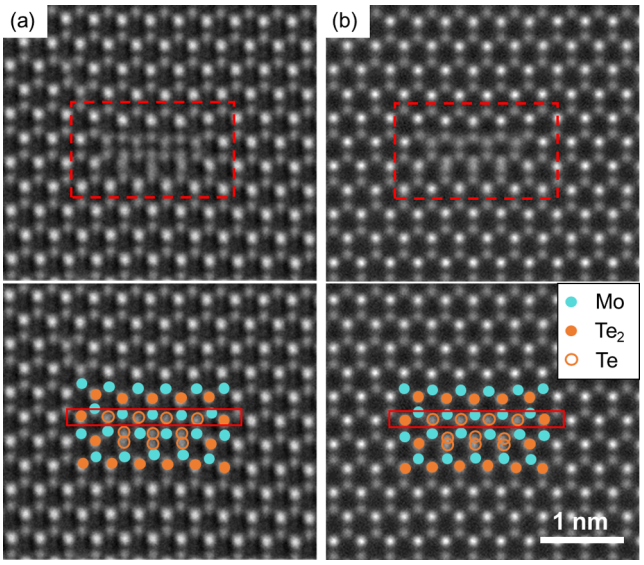

Figure 5. The 40 kV Cc/Cs-corrected HRTEM images of an experimental (a) and a simulated (b) single vacancy line with four missing Te atoms seen within the dashed frame in the upper images (and framed by their solid rectangular in the lower images). In the lower panels, atoms in the areas marked in upper image are highlighted with different colors: solid, orange dots mark two stacked-up Te atoms, orange rings mark one Te atom, and the turquoise solid dots mark Mo atoms.

tendency toward clustering of isolated vacancies can be investigated via the energy gain upon forming extended defects from isolated vacancies as a function of missing Te atoms. The negative values indicate the energy release when vacancies agglomerate into lines. It has been found that the vacancies are more prone to cluster along the zigzag direction than armchair direction. In the zigzag direction, Figure 6 d, the energy release is about 0.04 and 0.6 eV per Te atom for a single vacancy line and staggered divacancy line, respectively.

As compared to the zigzag direction (d), Te vacancy lines in the armchair direction (h) are energetically less favorable. The formation of the single Te vacancy line and the staggered Te divacancy line is endothermic and thus unlikely. Only the column Te divacancy line releases energy upon agglomeration of vacancies, as previously reported.[27] Overall, the formation of vacancy lines along the zigzag directions is energetically preferable compared to armchair direction.

The spin-polarized total density of states (DOS) was calculated for different line defects along the zigzag direction, shown in Figure 7. As can be seen, states appear which can be interpreted as band gap reduction as compared to the pristine structure of $MoTe_2$, providing that the concentration of vacancy lines is high. A similar effect on the band gap has been observed for vacancy lines along the armchair direction (Figure S7 in SI). However, line defects can be regarded as quantum wires because of confined metallic properties within the semiconducting $MoTe_2$. Spatial localization of spin up and down electron density indicates that some of these metallic structures, e.g., column Te divacancy line could be used in spintronics.

As evident from Figure 6, the most favorable configuration is staggered Te divacancy lines followed by single Te vacancy lines both in zigzag direction. In the experimental images, we found only zigzag single Te vacancy lines, although point defects of column Te divacancies were often observed, Figure

DOI: 10.1021/acsanm.9b00616
ACS Appl. Nano Mater. 2019, 2, 3262−3270

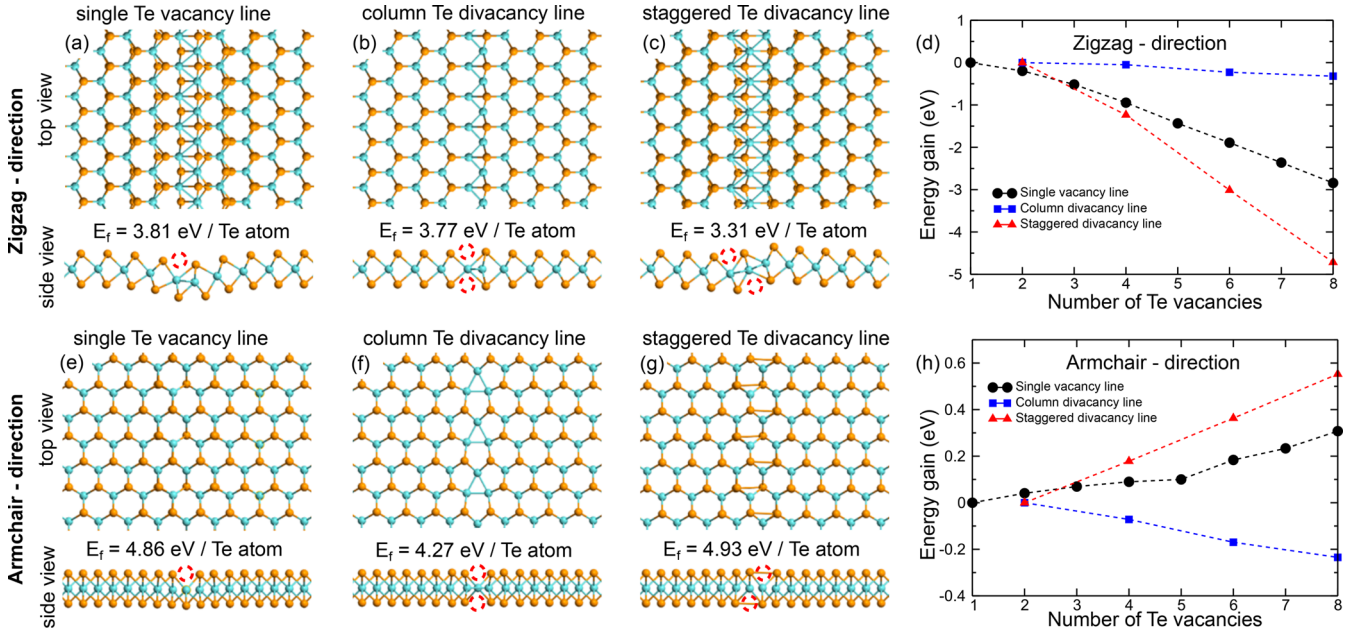

Figure 6. DFT calculations for vacancy lines. In (a–c), vacancy line structures oriented in zigzag direction and the corresponding formation energies E_f are presented. The energy gains upon forming extended defect from isolated vacancies are shown in (d) for vacancy lines of different lengths. The single vacancy line is energetically favorable up to a length of three vacancies, and afterward the staggered divacancy line has lower energy. The structure of vacancy lines and their formation energies in armchair direction are given in (e–g). In the side view of the atomic structures, the red dashed rings indicate the positions of the missing Te atoms. (h) The energy difference for the agglomerated lines in armchair directions. The only model, which yields energy gain upon agglomeration of vacancies, is the column divacancy line.

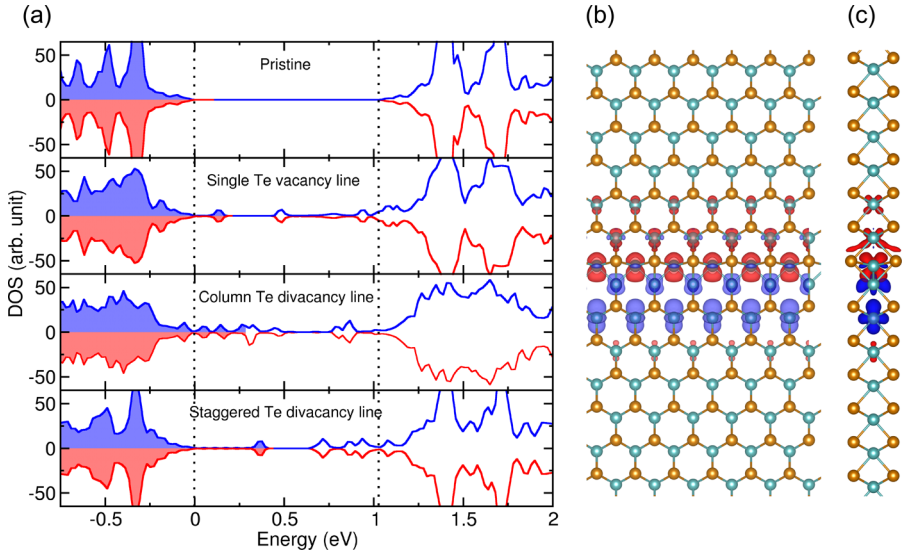

Figure 7. (a) Spin-polarized total density of states for various line defects in $MoTe_2$. The defect structures are oriented along the zigzag direction. The dotted lines show the band edges of the pristine system. (b,c) Spin density in column Te divacancy line. Blue and red colors correspond to the majority/minority spin densities, respectively, top (b) and side (c) views. The isosurface was set to 0.0003 e $Å^{-3}$.

2, while column or staggered Te divacancy lines were not present.

This observation and structural evolution of the defects under the electron beam can be understood in terms of the energetics of defects of various types. Figure 8 summarizes the formation energies for all defect structures including single vacancy lines, tetravacancies, and trefoil-like structures. In the case of the single Te vacancies, the formation of lines is energetically favored. In the case of column Te divacancies their agglomeration to lines is only slightly preferred. However, their agglomeration to extended point defects releases a substantial amount of energy, as schematically indicated by the dashed path in Figure 8. On the basis of the energetics, one can expect that two column Te divacancies directly form the tetravacancy II structure. Although, as described above, the tetravacancy II structure can only be reached via the tetravacancy I structure, which is metastable, so that the system prefers forming extended point defects, not column vacancy lines.

The formation of the trefoil defect is due to further clustering of column Te divacancies. It has a formation energy

DOI: 10.1021/acsanm.9b00616
ACS Appl. Nano Mater. 2019, 2, 3262–3270

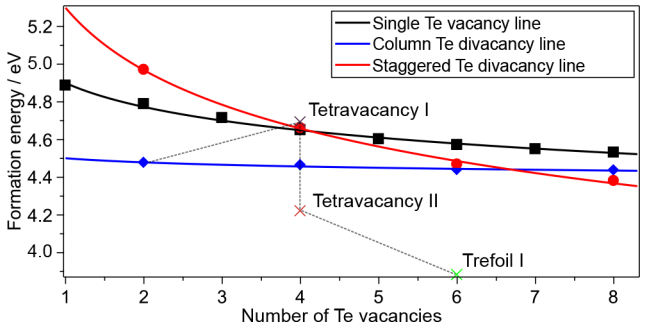

Figure 8. Formation energies of Te vacancy lines and extended defects as functions of the number of Te vacancies. A dashed path is added to illustrate and guide the eye along the agglomeration process of column Te divacancies.

of 3.88 eV per Te atom, so that it is strongly preferred over the Te divacancy line with the same number of missing atoms.

At higher vacancy concentrations, formation of inversion domains, Figure 9a–c, and local phase transformations from 2H to 1T′ $MoTe_2$ phase, Figure 9d–f, occurred. In the case of the inversion domains, the observed MTBs evolve due to Te deficiency and form 4|4P and 4|4E boundaries as shown in Figure 9b. The shown inversion domain appeared due to electron beam irradiation after a total accumulated dose of $\sim 1.4 \times 10^9$ e^-/nm^2. Formation of 4|4P MTBs due to thermal annealing which leads to Te deficiency, similar to our electron-beam irradiation, were earlier reported.[25] However, the 4|4E MTB (cf Figure 9b), based on Te deficiency was not observed earlier in $MoTe_2$. Panel (c) presents the same image as in panels (a) and (b) but, for better visualization, the atoms are colored: solid orange dots mark two stacked-up tellurium (Te_2) atoms and the blue solid dots mark Mo atoms. The red arrows in (a) and (c) indicate the corners of the inversion domain.

Figure 9d shows a single Te vacancy line with six missing Te atoms. The vacancy line is located between the red arrows. The displacements of Te atoms, indicated by white arrows, led to a formation of an island of 1T′ phase in (e). Furthermore, the single vacancy line moved along a distance of two unit cells. A white dashed trapezoid is fixed in (d) and (e) at the same position to clarify the change in the structure. Parts d and e of Figure 9 are consecutive images with exposure times of 1 s. Again, for better visualization, the atoms are colored in (f) like in (c) but this time also with the orange ring which marks a single Te atom. Similar transformations have been observed under electron beam in Redoped MoS_2.[3] The transformation likely originates from strain induced by vacancies and possibly other effects related to charge transfer and vibrational properties.[12,26,48]

CONCLUSIONS

Our Cc/Cs-corrected HRTEM experiments performed at an electron acceleration voltage of 40 kV revealed a plethora of point and line defects in the HRTEM images of monolayer $MoTe_2$, and together with first-principles simulations, provided insights into their formation and evolution process. We demonstrated that Te vacancies can agglomerate either in single Te vacancy lines or in extended defects composed of column Te vacancies, including rotational trefoil-like defects. Some of them, e.g., tetravcacancies I and II, have never been observed before. We also showed that the formation of inversion domains with mirror twin boundaries of different types, along with the islands of the metallic T′ phase can occur under the 40 kV electron beam. Our first-principles calculations provided insights into the energetics of the transformations as well as the electronic structure of the system with defects. Specifically, we point out that some of the observed defects have localized magnetic moments, which may add functionalities to 2D $MoTe_2$ through defect engineering. Our results indicate that various nanoscale morphologies,

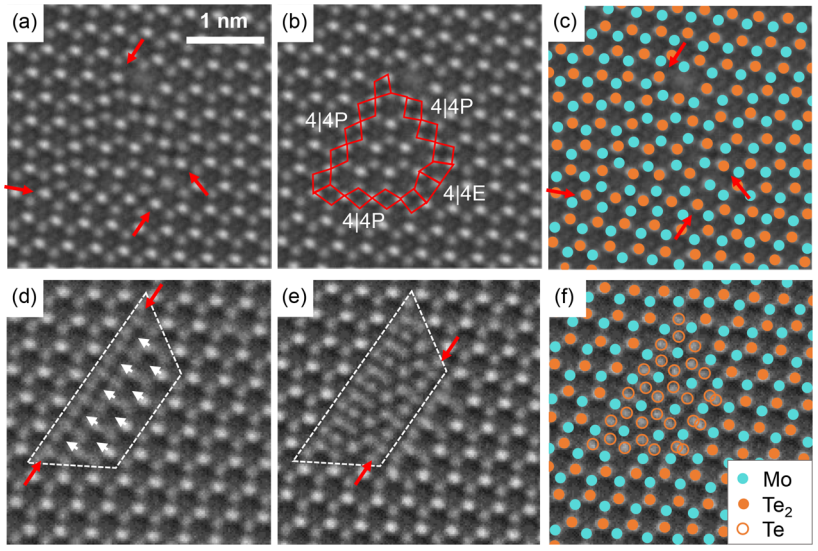

Figure 9. The 40 kV HRTEM images of inversion domains (a–c). In (a), the arrows indicate the corners of the inversion domain. The type of the MTBs is marked in (b) with the red lines and correspond to 4|4P and 4|4E boundaries. In (c), the atoms are marked with different colors: solid orange for Te_2 and solid turquoise for Mo atoms. The images (d–f) show a local phase transformation from the 2H to 1T′ phase. The atom migration indicated by white arrows is induced by a strain of a single Te vacancy line, located between the red arrows (d). Image (e) show the 1T′ phase. The white trapezoidal frame clarifies that the vacancy line is moved and it is shorter after the transformation. In (f), the atoms are again colored for better visualization.

DOI: 10.1021/acsanm.9b00616
ACS Appl. Nano Mater. 2019, 2, 3262–3270

including metallic islands of the T′ phase, and one-dimensional metallic systems based on vacancy lines and mirror twin boundaries embedded into a semiconducting host material can be realized in single-layer 2H $MoTe_2$. The former system can be referred to as a quantum dot, while the latter structure is very interesting in the context of fundamental aspects of the physics of Tomonaga−Luttinger liquid[49] and, as for practical aspects, plasmonics. Our calculations indicate that defect-associated magnetism can also be added to the system, which may lead toward control of optical and electronic properties for quantum devices in 2D materials.

■ ASSOCIATED CONTENT

Supporting Information

The Supporting Information is available free of charge on the ACS Publications website at DOI: 10.1021/acsanm.9b00616.

Additional information about 40 kV high-resolution TEM images with wide field of view, image simulations of tetravacancies I, and II and trefoil I, DFT based structure simulations of tetravacancies III and IV and trefoil II, DFT based structure simulations of vacancy lines with three vacancies perpendicular to the spreading direction, spin-polarized DOS for tetravacancies III and IV and trefoil II and vacancy lines in armchair direction (PDF)

■ AUTHOR INFORMATION

Corresponding Authors

*T.L.: E-mail, tibor.lehnert@uni-ulm.de.

*U.K.: E-mail, ute.kaiser@uni-ulm.de.

ORCID

Tibor Lehnert: 0000-0002-4904-9580

Mahdi Ghorbani-Asl: 0000-0003-3060-4369

Arkady V. Krasheninnikov: 0000-0003-0074-7588

Notes

The authors declare no competing financial interest.

■ ACKNOWLEDGMENTS

We acknowledge funding from the German Research Foundation (DFG) and the Ministry of Science, Research and the Arts (M.W.K.) of the federal state of Baden-Württemberg, Germany, in the frame of the SALVE (Sub Angström Low-Voltage Electron Microscopy) project (KA 1295/21-1) as well as the European Community in the frame of the Graphene Flagship. We acknowledge PRACE (HLRS, Stuttgart, Germany) for generous grants of CPU time. A.V.K. thanks the Academy of Finland for the support under project no. 286279 and the DFG under project KR 4866/1-1.

■ REFERENCES

(1) Chhowalla, M.; Shin, H. S.; Eda, G.; Li, L.-J.; Loh, K. P.; Zhang, H. The Chemistry of Two-Dimensional Layered Transition Metal Dichalcogenide Nanosheets. *Nat. Chem.* **2013**, *5* (4), 263.

(2) Manzeli, S.; Ovchinnikov, D.; Pasquier, D.; Yazyev, O. V.; Kis, A. 2D Transition Metal Dichalcogenides. *Nat. Rev. Mater.* **2017**, *2* (8), 17033.

(3) Lin, Y.-C.; Dumcenco, D. O.; Huang, Y.-S.; Suenaga, K. Atomic Mechanism of the Semiconducting-to-Metallic Phase Transition in Single-Layered MoS_2. *Nat. Nanotechnol.* **2014**, *9* (5), 391.

(4) Wilson, J. A.; Di Salvo, F. J.; Mahajan, S. Charge-Density Waves and Superlattices in the Metallic Layered Transition Metal Dichalcogenides. *Adv. Phys.* **1975**, *24* (2), 117−201.

(5) Wang, Q. H.; Kalantar-Zadeh, K.; Kis, A.; Coleman, J. N.; Strano, M. S. Electronics and Optoelectronics of Two-Dimensional Transition Metal Dichalcogenides. *Nat. Nanotechnol.* **2012**, *7* (11), 699.

(6) Keum, D. H.; Cho, S.; Kim, J. H.; Choe, D.-H.; Sung, H.-J.; Kan, M.; Kang, H.; Hwang, J.-Y.; Kim, S. W.; Yang, H.; Chang, K. J.; Lee, Y. H. Bandgap Opening in Few-Layered Monoclinic $MoTe_2$. *Nat. Phys.* **2015**, *11* (6), 482.

(7) Deng, K.; Wan, G.; Deng, P.; Zhang, K.; Ding, S.; Wang, E.; Yan, M.; Huang, H.; Zhang, H.; Xu, Z.; Denlinger, J.; Fedorov, A.; Yang, H.; Duan, W.; Yao, H.; Wu, Y.; Fan, S.; Zhang, H.; Chen, X.; Zhou, S. Experimental Observation of Topological Fermi Arcs in Type-II Weyl Semimetal $MoTe_2$. *Nat. Phys.* **2016**, *12* (12), 1105.

(8) Joshi, J.; Stone, I. R.; Beams, R.; Krylyuk, S.; Kalish, I.; Davydov, A. V.; Vora, P. M. Phonon Anharmonicity in Bulk Td-$MoTe_2$. *Appl. Phys. Lett.* **2016**, *109* (3), 031903.

(9) Tran, T. T.; Wang, D.; Xu, Z.-Q.; Yang, A.; Toth, M.; Odom, T. W.; Aharonovich, I. Deterministic Coupling of Quantum Emitters in 2D Materials to Plasmonic Nanocavity Arrays. *Nano Lett.* **2017**, *17* (4), 2634−2639.

(10) He, Y.-M.; Clark, G.; Schaibley, J. R.; He, Y.; Chen, M.-C.; Wei, Y.-J.; Ding, X.; Zhang, Q.; Yao, W.; Xu, X.; Lu, C.-Y.; Pan, J.-W. Single Quantum Emitters in Monolayer Semiconductors. *Nat. Nanotechnol.* **2015**, *10* (6), 497.

(11) Klinovaja, J.; Loss, D. Spintronics in MoS_2 Monolayer Quantum Wires. *Phys. Rev. B: Condens. Matter Mater. Phys.* **2013**, *88*, 075404.

(12) Duerloo, K.-A. N.; Li, Y.; Reed, E. J. Structural Phase Transitions in Two-Dimensional Mo-and W-Dichalcogenide Monolayers. *Nat. Commun.* **2014**, *5*, 4214.

(13) Wang, Y.; Xiao, J.; Zhu, H.; Li, Y.; Alsaid, Y.; Fong, K. Y.; Zhou, Y.; Wang, S.; Shi, W.; Wang, Y.; Zettl, A.; Reed, E. J.; Zhang, X. Structural Phase Transition in Monolayer $MoTe_2$ Driven by Electrostatic Doping. *Nature* **2017**, *550* (7677), 487.

(14) Cho, S.; Kim, S.; Kim, J. H.; Zhao, J.; Seok, J.; Keum, D. H.; Baik, J.; Choe, D.-H.; Chang, K. J.; Suenaga, K.; Kim, S. W.; Lee, Y. H.; Yang, H. Phase Patterning for Ohmic Homojunction Contact in $MoTe_2$. *Science* **2015**, *349* (6248), 625−628.

(15) Komsa, H.-P.; Krasheninnikov, A. V. Engineering the Electronic Properties of Two-Dimensional Transition Metal Dichalcogenides by Introducing Mirror Twin Boundaries. *Adv. Electron. Mater.* **2017**, *3* (6), 1600468.

(16) Seok, J.; Lee, J.-H.; Cho, S.; Ji, B.; Kim, H. W.; Kwon, M.; Kim, D.; Kim, Y.-M.; Oh, S. H.; Kim, S. W.; Lee, Y. H.; Son, Y.-W.; Yang, H. Active Hydrogen Evolution through Lattice Distortion in Metallic $MoTe_2$. *2D Mater.* **2017**, *4* (2), 025061.

(17) Kosmala, T.; Coy Diaz, H.; Komsa, H.-P.; Ma, Y.; Krasheninnikov, A. V.; Batzill, M.; Agnoli, S. Metallic Twin Boundaries Boost the Hydrogen Evolution Reaction on the Basal Plane of Molybdenum Selenotellurides. *Adv. Energy Mater.* **2018**, *8*, 1800031.

(18) Guguchia, Z.; Kerelsky, A.; Edelberg, D.; Banerjee, S.; von Rohr, F.; Scullion, D.; Augustin, M.; Scully, M.; Rhodes, D. A.; Shermadini, Z.; Luetkens, H.; Shengelaya, A.; Baines, C.; Morenzoni, E.; Amato, A.; Hone, J. C.; Khasanov, R.; Billinge, S. J. L.; Santos, E.; Pasupathy, A. N.; Uemura, Y. J. Magnetism in Semiconducting Molybdenum Dichalcogenides. *Sci. Adv.* **2018**, *4* (12), eaat3672.

(19) Ma, Y.; Kolekar, S.; Coy Diaz, H.; Aprojanz, J.; Miccoli, I.; Tegenkamp, C.; Batzill, M. Metallic Twin Grain Boundaries Embedded in $MoSe_2$ Monolayers Grown by Molecular Beam Epitaxy. *ACS Nano* **2017**, *11* (5), 5130−5139.

(20) Lehtinen, O.; Komsa, H.-P.; Pulkin, A.; Whitwick, M. B.; Chen, M.-W.; Lehnert, T.; Mohn, M. J.; Yazyev, O. V.; Kis, A.; Kaiser, U.; Krasheninnikov, A. V. Atomic Scale Microstructure and Properties of Se-Deficient Two-Dimensional $MoSe_2$. *ACS Nano* **2015**, *9* (3), 3274−3283.

(21) Barja, S.; Wickenburg, S.; Liu, Z.-F.; Zhang, Y.; Ryu, H.; Ugeda, M. M.; Hussain, Z.; Shen, Z.-X.; Mo, S.-K.; Wong, E.; Salmeron, M. B.; Wang, F.; Crommie, M. F.; Ogletree, D. F.; Neaton, J. B.; Weber-

DOI: 10.1021/acsanm.9b00616
ACS Appl. Nano Mater. 2019, 2, 3262−3270

Bargioni, A. Charge Density Wave Order in 1D Mirror Twin Boundaries of Single-Layer $MoSe_2$. *Nat. Phys.* **2016**, *12*, 751−756.
(22) Lin, Y.-C.; Björkman, T.; Komsa, H.-P.; Teng, P.-Y.; Yeh, C.-H.; Huang, F.-S.; Lin, K.-H.; Jadczak, J.; Huang, Y.-S.; Chiu, P.-W.; Krasheninnikov, A. V.; Suenaga, K. Three-Fold Rotational Defects in Two-Dimensional Transition Metal Dichalcogenides. *Nat. Commun.* **2015**, *6*, 6736.
(23) Lin, J.; Pantelides, S. T.; Zhou, W. Vacancy-Induced Formation and Growth of Inversion Domains in Transition-Metal Dichalcogenide Monolayer. *ACS Nano* **2015**, *9* (5), 5189−5197.
(24) Coelho, P. M.; Komsa, H.-P.; Coy Diaz, H.; Ma, Y.; Krasheninnikov, A. V.; Batzill, M. Post-Synthesis Modifications of Two-Dimensional $MoSe_2$ or $MoTe_2$ by Incorporation of Excess Metal Atoms into the Crystal Structure. *ACS Nano* **2018**, *12* (4), 3975−3984.
(25) Zhu, H.; Wang, Q.; Cheng, L.; Addou, R.; Kim, J.; Kim, M. J.; Wallace, R. M. Defects and Surface Structural Stability of $MoTe_2$ Under Vacuum Annealing. *ACS Nano* **2017**, *11* (11), 11005−11014.
(26) Elibol, K.; Susi, T.; Argentero, G.; Reza Ahmadpour Monazam, M.; Pennycook, T. J.; Meyer, J. C.; Kotakoski, J. Atomic Structure of Intrinsic and Electron-Irradiation-Induced Defects in $MoTe_2$. *Chem. Mater.* **2018**, *30* (4), 1230−1238.
(27) Zhao, J.; Nam, H.; Ly, T. H.; Yun, S. J.; Kim, S.; Cho, S.; Yang, H.; Lee, Y. H. Chain Vacancies in 2D Crystals. *Small* **2017**, *13* (1), 1601930.
(28) Pizzochero, M.; Yazyev, O. V. Point Defects in the 1 T′ and 2 H Phases of Single-Layer MoS_2: A Comparative First-Principles Study. *Phys. Rev. B: Condens. Matter Mater. Phys.* **2017**, *96* (24), 245402.
(29) Algara-Siller, G.; Kurasch, S.; Sedighi, M.; Lehtinen, O.; Kaiser, U. The Pristine Atomic Structure of MoS_2 Monolayer Protected from Electron Radiation Damage by Graphene. *Appl. Phys. Lett.* **2013**, *103*, 20307.
(30) Lehnert, T.; Lehtinen, O.; Algara–Siller, G.; Kaiser, U. Electron Radiation Damage Mechanisms in 2D $MoSe_2$. *Appl. Phys. Lett.* **2017**, *110*, 033106.
(31) Nguyen, L.; Komsa, H.-P.; Khestanova, E.; Kashtiban, R. J.; Peters, J. J. P.; Lawlor, S.; Sanchez, A. M.; Sloan, J.; Gorbachev, R. V.; Grigorieva, I. V.; Krasheninnikov, A. V.; Haigh, S. J. Atomic Defects and Doping of Monolayer $NbSe_2$. *ACS Nano* **2017**, *11*, 2894−2904.
(32) Wang, S.; Lee, G.-D.; Lee, S.; Yoon, E.; Warner, J. H. Detailed Atomic Reconstruction of Extended Line Defects in Monolayer MoS_2. *ACS Nano* **2016**, *10* (5), 5419−5430.
(33) Komsa, H.-P.; Kurasch, S.; Lehtinen, O.; Kaiser, U.; Krasheninnikov, A. V. From Point to Extended Defects in Two-Dimensional MoS_2: Evolution of Atomic Structure under Electron Irradiation. *Phys. Rev. B: Condens. Matter Mater. Phys.* **2013**, *88*, 035301.
(34) Zan, R.; Ramasse, Q. M.; Jalil, R.; Georgiou, T.; Bangert, U.; Novoselov, K. S. Control of Radiation Damage in MoS_2 by Graphene Encapsulation. *ACS Nano* **2013**, *7* (11), 10167−10174.
(35) Kaiser, U.; Biskupek, J.; Meyer, J. C.; Leschner, J.; Lechner, L.; Rose, H.; Stöger-Pollach, M.; Khlobystov, A. N.; Hartel, P.; Müller, H.; Haider, M.; Eyhusen, S.; Benner, G. Transmission Electron Microscopy at 20 KV for Imaging and Spectroscopy. *Ultramicroscopy* **2011**, *111* (8), 1239−1246.
(36) Linck, M.; Hartel, P.; Uhlemann, S.; Kahl, F.; Müller, H.; Zach, J.; Haider, M.; Niestadt, M.; Bischoff, M.; Biskupek, J.; Lee, Z.; Lehnert, T.; Börrnert, F.; Rose, H.; Kaiser, U. Chromatic Aberration Correction for Atomic Resolution TEM Imaging from 20 to 80 KV. *Phys. Rev. Lett.* **2016**, *117*, 076101.
(37) Lee, Z.; Meyer, J. C.; Rose, H.; Kaiser, U. Optimum HRTEM Image Contrast at 20 KV and 80 KV—exemplified by Graphene. *Ultramicroscopy* **2012**, *112* (1), 39−46.
(38) Blake, P.; Hill, E. W.; Castro Neto, A. H.; Novoselov, K. S.; Jiang, D.; Yang, R.; Booth, T. J.; Geim, A. K. Making Graphene Visible. *Appl. Phys. Lett.* **2007**, *91*, 063124.
(39) Benameur, M. M.; Radisavljevic, B.; Héron, J. S.; Sahoo, S.; Berger, H.; Kis, A. Visibility of Dichalcogenide Nanolayers. *Nanotechnology* **2011**, *22* (12), 125706.
(40) Perdew, J. P.; Burke, K.; Ernzerhof, M. Generalized Gradient Approximation Made Simple. *Phys. Rev. Lett.* **1996**, *77* (18), 3865.
(41) Kresse, G.; Furthmüller, J. Efficiency of Ab-Initio Total Energy Calculations for Metals and Semiconductors Using a Plane-Wave Basis Set. *Comput. Mater. Sci.* **1996**, *6* (1), 15−50.
(42) Monkhorst, H. J.; Pack, J. D. Special Points for Brillouin-Zone Integrations. *Phys. Rev. B* **1976**, *13* (12), 5188.
(43) Komsa, H.-P.; Kotakoski, J.; Kurasch, S.; Lehtinen, O.; Kaiser, U.; Krasheninnikov, A. V. Two-Dimensional Transition Metal Dichalcogenides under Electron Irradiation: Defect Production and Doping. *Phys. Rev. Lett.* **2012**, *109*, 035503.
(44) Meyer, J. C.; Eder, F.; Kurasch, S.; Skakalova, V.; Kotakoski, J.; Park, H. J.; Roth, S.; Chuvilin, A.; Eyhusen, S.; Benner, G.; Krasheninnikov, A. V.; Kaiser, U. Accurate Measurement of Electron Beam Induced Displacement Cross Sections for Single-Layer Graphene. *Phys. Rev. Lett.* **2012**, *108* (19), 196102.
(45) Cowley, J. M.; Moodie, A. F. The Scattering of Electrons by Atoms and Carystals. I. A New Theoretical Approach. *Acta Crystallogr.* **1957**, *10* (10), 609−619.
(46) Ghorbani-Asl, M.; Enyashin, A. N.; Kuc, A.; Seifert, G.; Heine, T. Defect-Induced Conductivity Anisotropy in MoS 2 Monolayers. *Phys. Rev. B: Condens. Matter Mater. Phys.* **2013**, *88* (24), 245440.
(47) Ataca, C.; Sahin, H.; Akturk, E.; Ciraci, S. Mechanical and Electronic Properties of MoS2 Nanoribbons and Their Defects. *J. Phys. Chem. C* **2011**, *115* (10), 3934−3941.
(48) Kretschmer, S.; Komsa, H.-P.; Bøggild, P.; Krasheninnikov, A. V. Structural Transformations in Two-Dimensional Transition-Metal Dichalcogenide MoS_2 under an Electron Beam: Insights from First-Principles Calculations. *J. Phys. Chem. Lett.* **2017**, *8* (13), 3061−3067.
(49) Jolie, W.; Murray, C.; Weiß, P. S.; Hall, J.; Portner, F.; Atodiresei, N.; Krasheninnikov, A. V.; Busse, C.; Komsa, H.-P.; Rosch, A.; Michely, T. Tomonaga-Luttinger Liquid in a Box: Electrons Confined within MoS_2 Mirror-Twin Boundaries. *Phys. Rev. X* **2019**, *9* (1), 011055.

DOI: 10.1021/acsanm.9b00616
ACS Appl. Nano Mater. 2019, 2, 3262−3270